PCCP

PAPER

Identification of Au–S complexes on Au(100)†

Holly Walen,[a] Da-Jiang Liu,[b] Junepyo Oh,[c] Hyun Jin Yang,‡[c] Yousoo Kim[c] and P. A. Thiel*[abd]

Cite this: *Phys. Chem. Chem. Phys.*, 2016, **18**, 4891

Received 17th December 2015, Accepted 14th January 2016

DOI: 10.1039/c5cp07817b

www.rsc.org/pccp

Using a combination of scanning tunneling microscopy and density functional theory (DFT) calculations, we have identified a set of related Au–S complexes that form on Au(100), when sulfur adsorbs and lifts the hexagonal surface reconstruction. The predominant complex is diamond-shaped with stoichiometry Au_4S_5. All of the complexes can be regarded as combinations of S–Au–S subunits. The complexes exist within, or at the edges of, p(2 × 2) sulfur islands that cover the unreconstructed Au regions, and are observed throughout the range of S coverage examined in this study, 0.009 to 0.12 monolayers. A qualitative model is developed which incorporates competitive formation of complexes, Au rafts, and p(2 × 2) sulfur islands, as Au atoms are released by the surface structure transformation.

1. Introduction

In surface science, complexation reactions between adsorbates and indigenous surface metal atoms are reported with increasing frequency. Such complexes can influence metal mass transport,[1,2] engender exotic organometallic nanoarchitectures,[3–5] and allow control of surface properties by tuning the availability of metal atoms.[6]

In this paper we present evidence for a new type of complex that forms between S and Au atoms on Au(100). The interaction of S with Au surfaces is important because it is the most basic prototype for a large class of systems in which the S–Au bond anchors molecular ligands. These ligands range from (functionalized) alkyl groups[7–9] to biological molecules.[10,11] Such systems have many potential or real uses, such as detection of antibiotic-resistant bacteria[12] or fabrication of thin film transistors.[13] There is evidence that some of these molecular adsorbates can also form complexes with Au atoms *via* the S group.[14,15] In this vein, a "staple" motif has been reported whose basis is a linear S–Au–S subunit. As the name implies, the Au atom interacts weakly with the metal substrate in comparison to the S atoms, which are the ends of the staple.[15–17]

Previously, we reported that unexpected complexes can form between sulfur atoms and metal atoms on Ag(111)[18] and Cu(111),[19,20] with stoichiometries $Ag_{16}S_{13}$ and Cu_2S_3, respectively. Surprisingly, we found no evidence for complexation on Au(111) under similar conditions, although another group[21] did report some evidence for Au–S clusters. While the Ag and Cu moieties are very different from one other, they possess features that we attributed to certain common principles of formation: high metal coordination around one or more sulfur atoms, and/or linear S–M–S subunits (M = Cu, Ag). The latter resemble the staple units mentioned above.

The specific system described in this paper, sulfur on Au(100), has been characterized previously using STM, low-energy electron diffraction, and other techniques, in ultrahigh vacuum (UHV) and in electrochemical environments. It has been characterized over a large coverage range, and often at room temperature. The clean surface is hexagonally (hex) reconstructed, with an atomic density 25% higher than that of the unreconstructed (1 × 1) phase (*e.g.* ref. 22–30). Adsorption of sulfur causes the hex structure to revert to the (1 × 1), with the concomitant release of excess Au atoms.[31–34] Depending on temperature, some of the excess Au can coalesce into single layer islands (rafts) on the terraces.[31] Sulfur forms ordered structures on the unreconstructed regions, including a p(2 × 2),[31,32] c(2 × 6),[33] c(2 × 4),[31] ($\sqrt{2}$ × $\sqrt{2}$),[34] and an octomer phase.[34] Of these, the p(2 × 2) has the lowest ideal coverage (0.25 ML) and is most relevant to our work. It is a chemisorbed phase, with sulfur adsorbed in alternating four-fold hollow (4fh) sites.[35,36] Notably, Jiang *et al.*[31] observed that the p(2 × 2) appears immediately wherever the reconstruction is lifted, and that it covers both levels—terraces and rafts—of unreconstructed Au.

Our work includes a combination of scanning tunneling microscopy (STM) and density functional theory (DFT) calculations. The experimental work differs from prior work[31–34] in that conditions are designed to isolate possible complexes. Thus, S coverage is kept low to circumvent adsorbate-induced reconstructions, and the

[a] *Department of Chemistry, Iowa State University, Ames, Iowa 50011, USA. E-mail: pthiel@iastate.edu*
[b] *Ames Laboratory of the USDOE, Ames, Iowa 50011, USA*
[c] *Surface and Interface Science Laboratory, RIKEN, Wako, Saitama 351-0198, Japan*
[d] *Department of Materials Science & Engineering, Iowa State University, Ames, Iowa 50011, USA*

† Electronic supplementary information (ESI) available. See DOI: 10.1039/c5cp07817b

‡ Current address: University College London, London WC1E 6BT, UK.

observation temperature is low (5 K) to ensure immobilization of adsorbed species following S adsorption at 300 K. A new, diamond-shaped complex is very common under these experimental conditions. Using DFT, we calculate the relative stability of candidate structures, and we compare each candidate's physical characteristics—shape, size, and orientation—with experimental data. The methodologies of experiments and calculations are similar to those described elsewhere.[19,20,37,38]

The manuscript is organized as follows. Section 2 provides experimental and computational details. Section 3 presents experimental results, along with DFT-guided interpretation. The clean surface is described first, followed by features that develop as the reconstruction is lifted. These are p(2 × 2) islands, Au rafts, possibly S atoms on hex regions, S-decorated step edges, and complexes. The propensity for ejected Au atoms to reach step edges is then analyzed. Section 4 is a discussion of results, including connections with prior work, followed by concluding remarks in Section 5.

2. Experimental and computational details

2.1 Experimental description

The experimental instrumentation and procedures were similar to those used previously, in studies of S adsorption on Ag(111),[18] Cu(111),[19,20,39] Au(111),[37] and Au(110).[40] In the current work, the single crystal Au(100) sample was cleaned *via* several Ar^+ sputtering (10–15 μA, 1.5 kV, 10 min) and annealing (720 K, 10 min) cycles.

Imaging by STM was performed at 5 K in UHV, at pressure $<6.0 \times 10^{-11}$ Torr. Sulfur was deposited *in situ via* an electrochemical Ag|AgI|Ag_2S|Pt source.[41–43] The sample was held at 300 K during S deposition, and then cooled to 5 K for measurement. Cooling and stabilization for STM measurements was completed in approximately 50 minutes. After initial STM measurements, the sample was warmed back to room temperature and re-cooled to 5 K for further imaging, with no difference in the results. Tunneling conditions during imaging were in the range −1.00 V to +1.00 V sample bias (V_S), and 1.00 to 3.10 nA tunneling current (I). The ESI† gives tunneling conditions for each image.

The STM piezoelectric calibration was checked by comparing measured and predicted atomic dimensions. The atomic separation along the close packed directions, a, was measured as 0.282 ± 0.007 nm, and the step heights as 0.19 ± 0.02 nm. The in-plane lattice constant predicted for Au(111) is 0.288 nm;[44] there is a 4% contraction associated with the hex Au(100) surface,[27,45,46] which brings this value to 0.276 nm. The step height predicted from the bulk parameter is 0.204 nm.[44] Both are within one standard deviation of the measured values.

Sulfur coverage (θ_S) was obtained by counting protrusions in STM images (associating each small protrusion with a single S adatom, and each diamond-shaped protrusion with 5 S), and dividing by the areal density of atoms in a bulk Au(100) plane. This yielded coverage in units of absolute monolayers (ML). Five experiments were performed, spanning the coverage range 0.009 to 0.12 ML.

2.2 Computational description

We performed density functional theory (DFT) calculations using the VASP[47–49] package and the projected-augmented wave (PAW)[50] method. If not otherwise noted, the Perdew–Burke–Ernzerhof (PBE)[51] approximation was used for the exchange–correlation. Technical details can be found in ref. 19 and 38. Energetics were averaged over slabs with thickness, L, from 7 to 12 Au layers.[52] We used k-point grids that approximately corresponded to (24 × 24 × 1) for the primitive substrate cell. All configurations reported herein were energy-optimized, with the bottom layer of Au atoms fixed. STM images were generated from optimized configurations by taking the isosurface of partial charge density in an energy window that bracketed the Fermi energy by ±0.1 eV, after Tersoff and Hamann.[53]

We used DFT to evaluate the relative stability of S—either in the form of complexes or as chemisorbed adatoms—on the unreconstructed Au substrate. The metric is a chemical potential, μ_S, for S (at 0 K), which we have employed in several similar systems.[19,20,37,40] It is defined as

$$\mu_S = [E(Au_mS_n + \text{slab}) - E(\text{slab}) - m\mu_{Au}]/n - E(S_{2,g})/2 \quad (1)$$

where E is energy and μ_{Au} is the chemical potential of Au in the bulk metal (at 0 K), which also corresponds to the bulk cohesive energy. If bulk and surface are equilibrated, μ_{Au} is equivalent to the binding energy of a Au atom at a step kink site.[54] The integers m and n are the number of Au and S atoms in the complex, respectively. When m = 0, μ_S is simply the adsorption energy of a S adatom. Physically, μ_S reflects the energy increase per S, when atomic S on terraces is incorporated into complexes in the presence of an unlimited supply of Au available from steps/kinks. Eqn (1) defines the energy of gaseous triplet S_2 as the reference point for μ_S.

The size of the supercell can influence μ_S because of interactions between neighboring adsorbates. We therefore compare μ_S of the most important species at different supercell sizes (different θ_S). Whenever a value of μ_S is given, either the supercell or θ_S is specified. The area of the supercell is n/θ_S.

The most pertinent DFT results are presented in this text. Many others are provided in the ESI.†

3. Results

3.1 Clean surface

Fig. 1 shows STM images of the clean Au(100) surface. The characteristic hex reconstruction is visible at low magnification as long modulated stripes, parallel to either the [01$\bar{1}$] or [011] directions. Fig. 1(a) shows a stepped region that encompasses both types of domains.

Fig. 1(b and c) resolves individual atoms and their hexagonal-like packing in the corrugated surface layer. The modulation of the stripes is mainly due to mismatch between close-packed rows of Au atoms in the (denser) hexagonal layer and in the unreconstructed layer beneath. The period of modulation is 7.57 ± 0.08 nm (based on the number, N, of 13 measurements), which spans about 27 Au

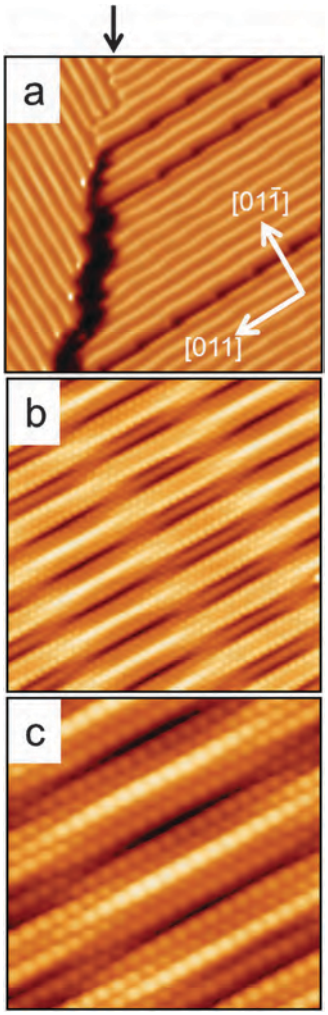

Fig. 1 STM images of a clean Au(100) surface. (a) Several step edges, and a domain boundary indicated with an arrow. The image is differentiated to facilitate viewing of hex stripes on different terraces; 30 × 30 nm^2. (b) Topographic image of a terrace region; 10 × 10 nm^2. (c) Topographic image of a terrace region with atomic resolution; 5 × 5 nm^2.

atoms in the top layer along the close-packed direction. These terrace images are very similar to those that have been reported and analyzed for the hexagonally reconstructed surfaces of Pt(100)[24,55,56] and Au(100).[26,31]

3.2 Features associated with chemisorbed sulfur

p(2 × 2) phase. As noted in Section 1, the p(2 × 2) is a known chemisorption phase with an ideal coverage of 0.25 ML, wherein S occupies 4fh sites on the unreconstructed Au(100) surface.[35,36] The following observations shed additional light on this structure, and provide context relevant to the surface complexes.

In our work, the p(2 × 2) is visible in localized regions even at the smallest total coverage, 0.009 ML. (We call such areas islands of p(2 × 2) phase.) The smallest p(2 × 2)-related islands are single rows of spots, separated by 2*a*, on a dark background which we take to be the unreconstructed metal. Examples are shown in Fig. 2(a and b). Some such rows adjoin a terminated

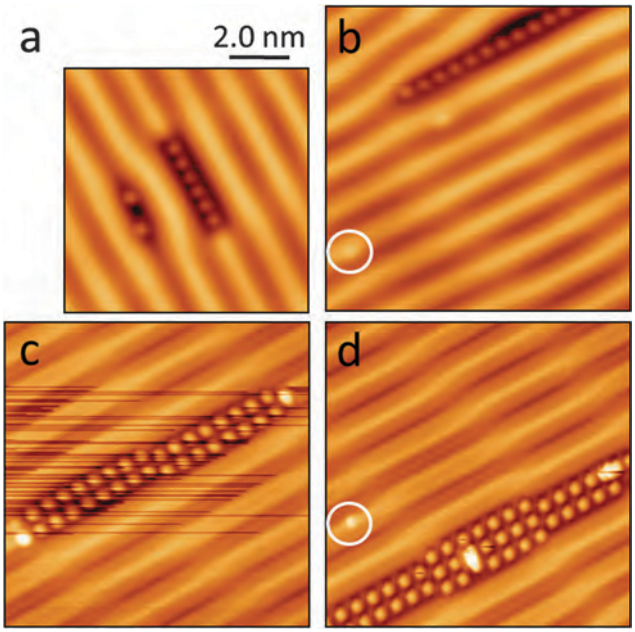

Fig. 2 One-dimensional rows and p(2 × 2) islands of sulfur atoms at 0.009 ML. All images are topographic and sized to the same scale. (a) 8.0 × 8.0 nm^2, (b) 10 × 10 nm^2, (c) 10 × 10 nm^2, (d) 10 × 10 nm^2.

hex stripe, and others are embedded in hex stripes that curve around them. Both cases can be seen in Fig. 2(a). Far more common than single rows are anisotropic p(2 × 2) islands like those in Fig. 2(c and d), each consisting of 2–3 rows. The anisotropy is clearly enforced by the surrounding hex orientation, since the long dimension of each p(2 × 2) island lies parallel to the hex stripes. The height and width of the protrusions (shown in Table 1) are comparable to S adatom dimensions we have measured in other systems under similar conditions.[37,40] Fig. 2(a) includes a pair of S atoms in a dark trough that may result from the dissociation of a single S_2 molecule, but this type of configuration was observed only once. Domain boundaries in the p(2 × 2) are very common.

Au rafts. As sulfur coverage increases up to 0.12 ML, the p(2 × 2) domains become larger and more isotropic, and rectangular rafts of Au form, adjacent to or inside the p(2 × 2) domains, as shown in Fig. 3. The rafts' identity is confirmed by the fact that their height, 0.18 ± 0.01 nm, equals the measured Au(100) step height, 0.19 ± 0.02 nm. These Au rafts are covered with the p(2 × 2) phase of S, and their edges align with the p(2 × 2) on lower terraces. All of these characteristics of Au rafts are consistent with the prior report of Jiang *et al.*[31]

S atoms on the hex phase. Occasionally, protrusions are observed on the hex phase that may be S atoms. Two are encircled in Fig. 2. They are always slightly off-center from a hex stripe, but their size is irregular. Their density is extremely low, with an estimated upper limit of 0.004 nm^{-2} at a total coverage of 0.009 ML, or 1 protrusion for every 400 Au atoms in the hex phase. Given the low density, we cannot exclude the possibility that some or all of these features are impurities.

DFT of the p(2 × 2) phase. We use DFT to evaluate μ_S (described in Section 2.2) of the chemisorbed phase. Fig. 4 shows

Table 1 Dimensions of features observed with STM, measured over sample bias from −1.00 to +1.00 V. The number of measurements is *N*

Assignment	Height, nm	Width at half-maximum, nm	*N*
S adatoms on terraces in p(2 × 2)	0.022 ± 0.004	0.293 ± 0.023	170
Au_4S_5 complexes (diamonds)	0.145 ± 0.020	Diagonal width: 1.04 ± 0.09 Narrowest width: 0.813 ± 0.077	58
AuS_2 complexes (oblongs)	0.114 ± 0.038	Length: 0.782 ± 0.059 Width: 0.508 ± 0.058	17

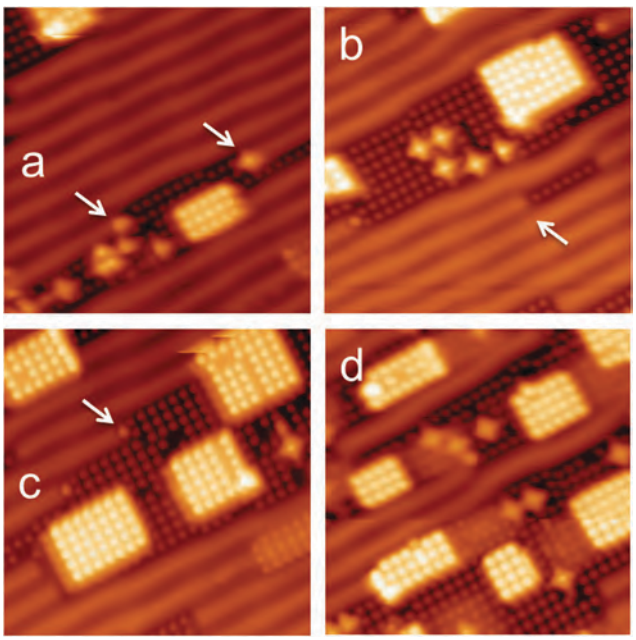

Fig. 3 Topographic images of Au rafts and complexes on the p(2 × 2) domains. The image size is 15 × 15 nm^2. (a) 0.024 ML, (b) 0.032 ML, (c) 0.055 ML, (d) 0.12 ML. Arrows are explained in the text.

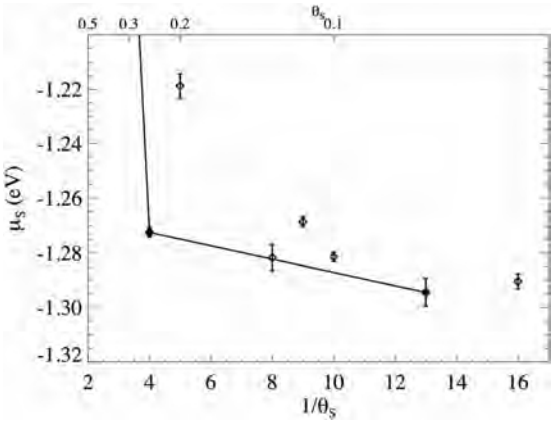

Fig. 4 Chemical potential of S chemisorbed on 4fh sites of Au(100) in 7 different supercells from DFT-PBE calculations.

Table 2 Pairwise interaction energies between neighboring S atoms. w_n represents the *n*-th nearest-neighbor interaction energy, derived for a lattice-gas model with only pair-wise interactions

n	1	2	3	4	5	6	7	8
w_n (eV)	0.433	0.211	0.001	0.031	0.006	0.012	0.005	−0.003

values of μ_S for S adatoms at the 4fh site on unreconstructed Au(100) surfaces for several different S configurations. Exact values of μ_S, together with other details, are given in the ESI.† Three of the values define a convex hull, shown by the solid line segments in Fig. 4. We call this envelope the baseline energetics. Consistent with experiment, the p(2 × 2) defines the minimum energy at 0.25 ML.

As an aside, Table 2 gives nearest-neighbor interaction energies, w_n (n = nearest-neighbor separation in units of a) calculated for a lattice-gas model with only pair-wise interactions, on the unreconstructed (100) surface. Interactions through the 7th nearest neighbor are all repulsive (positive), with w_3 lowest, consistent with p(2 × 2) ordering. Interestingly, the first four pairwise interaction energies are similar to those deduced by Bak *et al.*[57] for Se/Ni(100), where the experimental phase diagram also contains a p(2 × 2) phase. We also note that another DFT study[35] of S/Au(100) found similar values for w_1 and w_2, and postulated oscillatory longer-ranged interactions. In contrast, we observe only repulsive interactions up to 4a, but with especially strong repulsion for w_4.

S-Decorated step edges. At the lowest sulfur coverage investigated, 0.009 ML, step edges parallel to the hex stripes can be found that are decorated by single rows of protrusions, separated by $2a \approx 0.57 \pm 0.01$ nm (see Fig. 5(a)). These rows apparently evolve into p(2 × 2) domains of increasing size as sulfur coverage increases, based on images such as the one in Fig. 5(b). At a given coverage, the p(2 × 2) domains near steps are generally larger than those far from steps.

DFT-derived values of μ_S are shown in Fig. 6, for a row of S atoms in several locations near an unreconstructed step edge. The step edge is modeled by a 3-atom-wide Au strip in a (2 × 6) supercell. Fig. 6(a and b) show that a row of S adsorbed in 4fh sites on the lower terrace near a step is less stable than in pseudo-3-fold hollow sites directly at the step. Most favorable is the 4fh site along the upper terrace, adjacent to the edge, shown in Fig. 6(c). Adding an extra row of S on the lower terrace, as shown in Fig. 6(d), destabilizes the configuration based on the increase in μ_S. We conclude that the configuration with S atoms in 4fh sites on the upper terrace probably corresponds to the experimental image of Fig. 5(a).

3.3 Au–S complexes

Discrete features with well-defined shapes, other than those attributable to chemisorbed S, coexist with the p(2 × 2) phase even at the lowest measured coverage. The most common such features are diamond-shaped with a central bright spot.

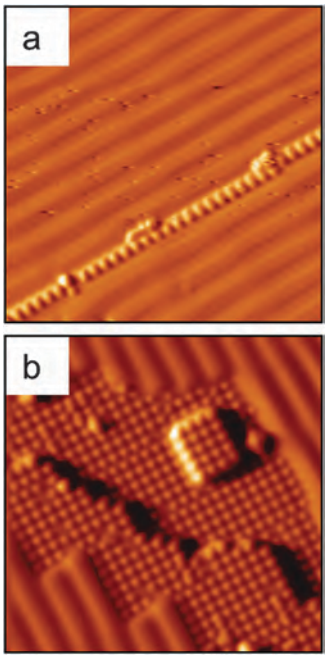

Fig. 5 STM images near step edges following adsorption of sulfur. Images are differentiated to facilitate viewing structures on different levels, and are 15×15 nm^2. (a) A row of sulfur at a step edge, 0.009 ML. Sulfur atoms are separated by 2*a*. (b) A step edge bounded by relatively large p(2 × 2) domains, 0.055 ML.

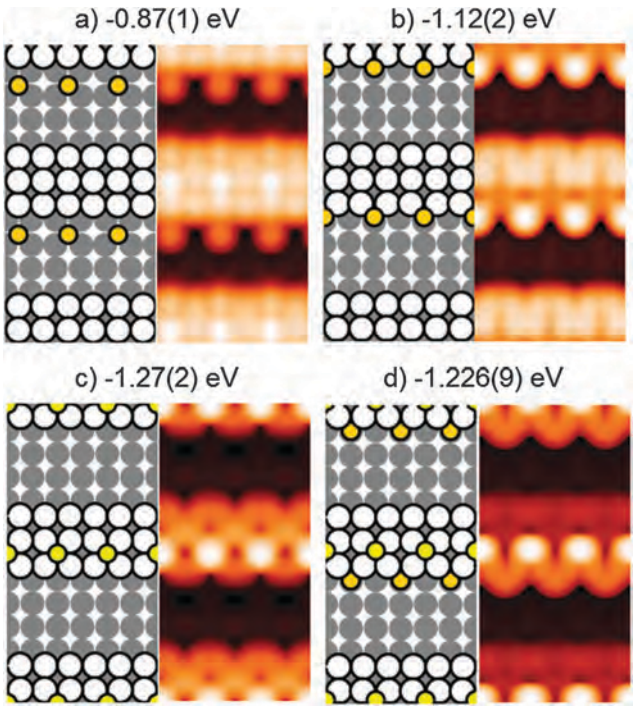

Fig. 6 Energy-optimized configurations, simulated STM images, and calculated chemical potentials of S rows at step edges. Gray circles represent Au atoms in the unreconstructed (100) surface; white circles are Au atoms on top of the (100) surface, representing a short-range gold terrace; gold circles are S atoms along the lower terrace, roughly coplanar with the Au atoms; and yellow circles are S atoms on the upper terrace. The supercells are (2 × 6).

Dimensions are given in Table 1. We assign these as Au_4S_5 complexes for reasons given below. Features also exist that resemble incomplete diamonds, although these are less common. Still less common are oblong features. All are visible in Fig. 7. For instance, arrows point to features with 3 and 2 vertices in Fig. 7(e) and Fig. 7(a and b), respectively, and to oblong shapes in Fig. 7(c).

We assign the complexes on the basis of DFT calculations represented in Fig. 8. Given the predominance of the p(2 × 2) phase in experiment, values of μ_S close to 0.25 ML are most relevant. At coverages close to 0.25 ML, several Au–S structures are more stable than the chemisorbed phase, by substantial margins: Au_4S_5, Au_3S_4, Au_2S_3, and AuS_2. These are represented by the points below the solid line in Fig. 8, and are shown schematically in Fig. 9. At 0.25 ML, the two most stable structures are Au_4S_5 and Au_3S_4, which both have μ_S about 0.15 eV below baseline.

The structure of the most-stable Au_4S_5 complex is shown in the upper part of Fig. 10(a). It consists of a square of 4 Au atoms, each positioned close to 2-fold bridge sites on the underlying Au substrate. This square supports a single S atom, forming a pyramid. In addition, 4 S atoms are at the corners of the Au base, which accounts for the diamond-like shape. It can be regarded as a central S atom with 4 AuS legs. Intuitively, one might expect that the 4 S atoms would instead be located along the sides of the Au base, as in Fig. 10(c). However, the side location is far less favorable, since μ_S is higher for that configuration by 0.86 eV. The presence of a S adatom close to Au_4S_5 (within 1.5 lattice constants of a corner S) makes surprisingly little difference to μ_S, based on the configuration in Fig. 10(b). This is consistent with the observation that Au_4S_5 complexes are embedded within the p(2 × 2) phase (although the p(2 × 2) is usually rather disordered in the near vicinity of a complex). The addition of more Au atoms to the Au base destabilizes the Au_4S_5 complex by over 0.4 eV, as illustrated in Fig. 10(d).

There is excellent agreement between STM images predicted from the DFT-optimized structure of Au_4S_5 and those measured experimentally, as seen by comparing the lower portions of Fig. 10(a and b) with Fig. 10(e). First, the distinctive shape is present in both cases: a bright central protrusion with 4 legs. In contrast, the configurations in Fig. 10(c and d) fail to reproduce this shape. Second, the orientation of the diamond is correct. To show this, the experimental image in Fig. 10(e) is rotated to align the underlying substrate (determined from the p(2 × 2)) with the substrates in Fig. 10(a–d). Third, the lateral dimensions of Au_4S_5 are comparable in theory and experiment. This can be confirmed by inspecting the sizes of the diamond-shaped features in the respective parts of Fig. 10, knowing that the size of the experimental image has been adjusted to match the scale of the DFT configurations—again, using the p(2 × 2) as guide. In both experiment and theory, the diagonal dimension spans about 4*a* or, in terms of the metric that is most available from the STM images, about 2 p(2 × 2) lattice constants.

The other features observed in STM can be considered partial diamonds that have 3 to 1 AuS legs emanating from the central S adatom. Energy-optimized configurations, STM images (both simulated and experimental), and the corresponding

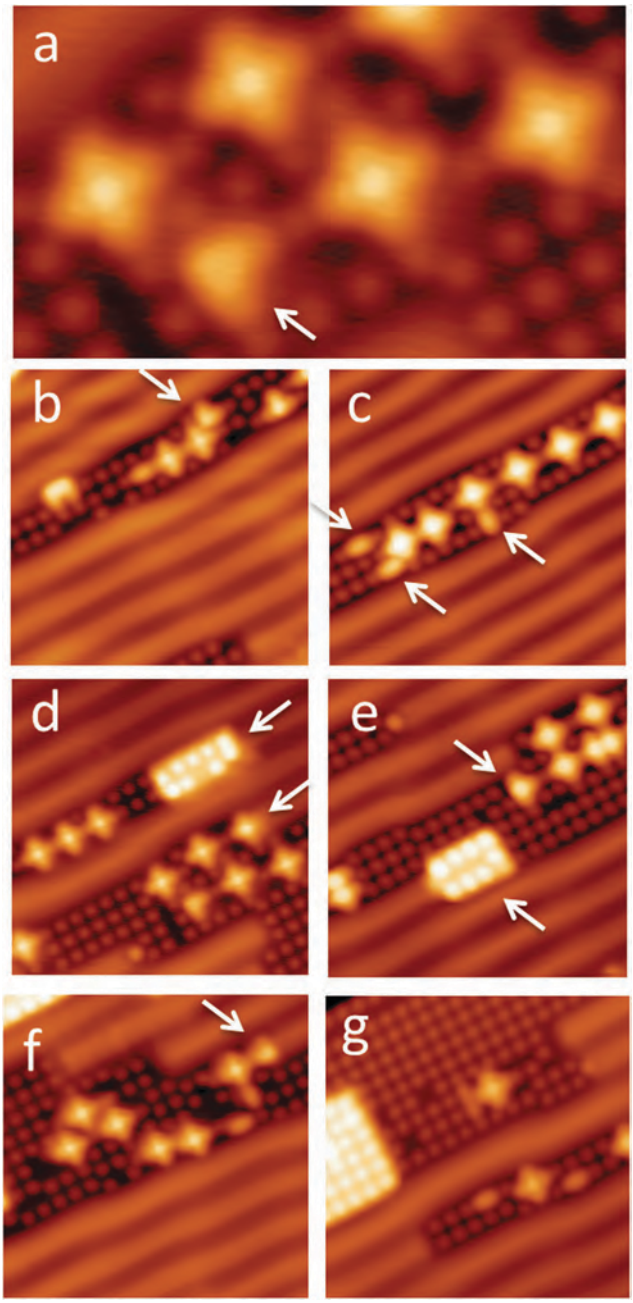

Fig. 7 Au–S complexes on p(2 × 2) domains. The image size of panel (a) is 5 × 3.3 nm^2; all others are 10 × 10 nm^2. (a) High resolution image of the Au_4S_5 complexes. The arrow indicates an Au_2S_3 complex. Sulfur coverage is 0.055 ML in all panels except (b and c), where it is 0.009 ML. The text explains the significance of the arrows.

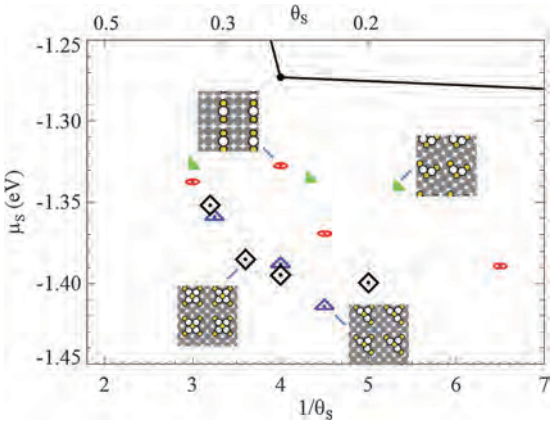

Fig. 8 Chemical potentials of most favorable complexes calculated from DFT. A portion of the convex hull for the chemisorbed phases, shown in Fig. 4, is reproduced by the black line segments. Red ovals indicate AuS_2, green triangles Au_2S_3, blue triangles Au_3S_4, and black lozenges Au_4S_5.

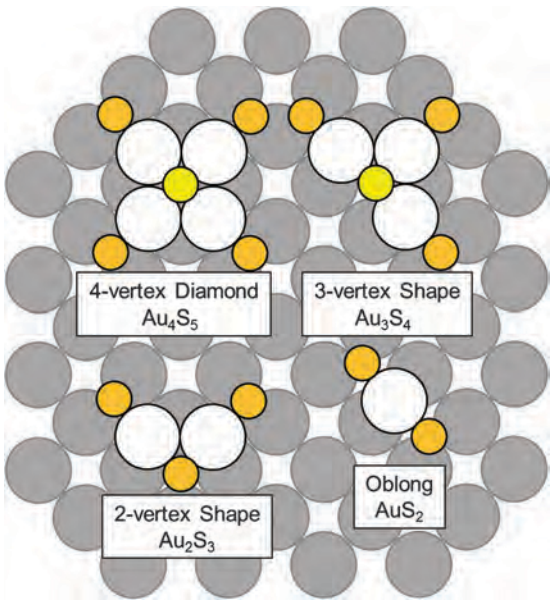

Fig. 9 Schematic representation of Au–S configurations, where gray circles represent Au atoms in the unreconstructed (100) surface; white circles are Au atoms on top of the (100) surface, as part of complexes; gold circles are S atoms in the complex, roughly coplanar with the Au atoms; and yellow circles are S atoms in an upper level, at the top of the complex.

chemical potentials are given in Fig. 11. The 3-leg structure is T-shaped, the 2-leg structure is heart-shaped, and the 1-leg structure is oblong shaped. In all complexes, the Au atoms are not at the natural 4fh sites, but rather at 2-fold bridge sites in the Au substrate, or nearly so; this is also evident in Fig. 9.

Values of chemical potential are compared in Fig. 8 for complexes with different numbers of AuS legs, for coverages close to 0.25 ML. In this coverage regime, complexes with 4 and 3 legs have comparable values of μ_S. Structures with 2 or 1 legs are less favored but still more stable than the p(2 × 2) phase.

Fig. 11 shows that 4- and 3-leg structures have the central S atom above the plane of the Au base and this makes the center of these complexes appear bright in the STM images. In the 2- and 1-leg structures, all S atoms are nearly co-planar with the remaining Au base, and so they lack the bright spot. Further insight into the structures of the two larger complexes, Au_4S_5 and Au_3S_4, is provided by the cross-sectional view in Fig. 12. This view shows that they can be regarded as slightly bent S–Au–S motifs in which one S adatom is lifted above the surface. The S–Au–S angles are 167.4° in Au_4S_5, and 172.4°

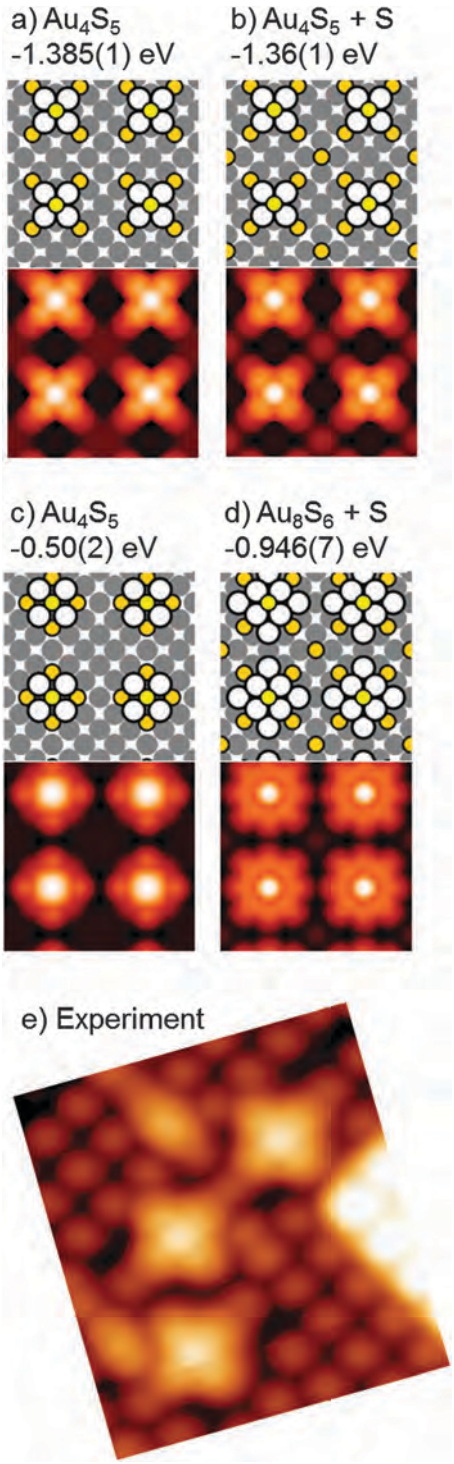

Fig. 10 Complexes related to diamond-shaped clusters. Top panels of (a—d) show energy-optimized configurations with the same color coding as in Fig. 9, and values of μ_S. Bottom panels show the corresponding STM images simulated from DFT. Panel (e) is an experimental image, size 3.6 × 4.0 nm^2, 0.12 ML.

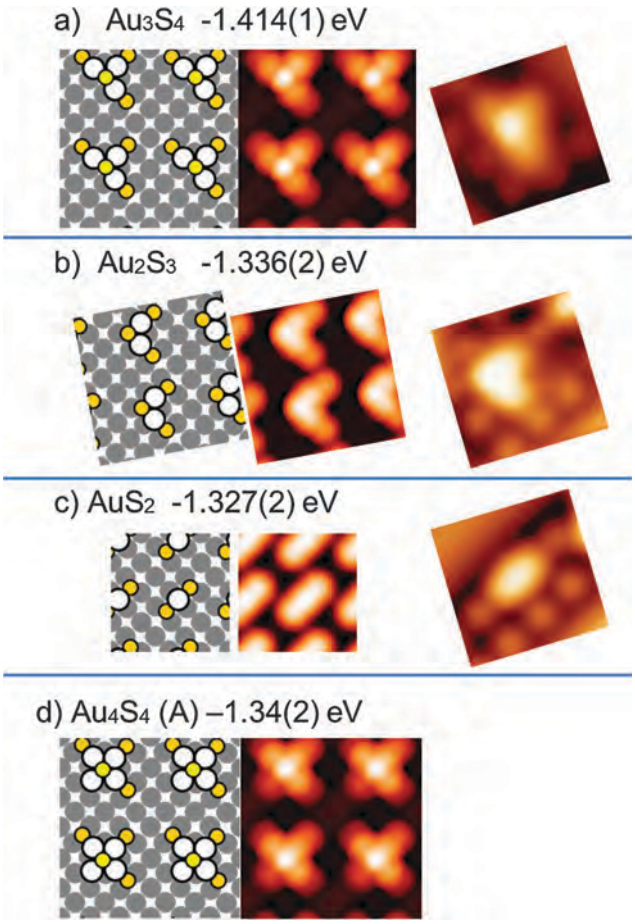

Fig. 11 Complexes related to partial diamonds. Each panel contains, from left to right: the energy-optimized configuration from DFT (with the same color coding as in Fig. 9); the corresponding simulated STM image; and the experimental STM image (2 × 2 nm^2), where applicable.

and 164.6° in Au_3S_4. In the latter case, the smaller angle is associated with the two AuS legs that point in opposite directions, *i.e.* the legs perpendicular to the plane of Fig. 12(a).

It is interesting that, starting from the 4-leg complex, smaller structures are generated by successively deleting the entire AuS legs. One might expect corner S atoms to be deleted instead, thus preserving the Au_4 base. However, the latter expectation is not supported by the values of μ_S. For example, the configuration in Fig. 11(d), which lacks a single corner S atom, is less stable by 0.09 eV than that in Fig. 11(a), which lacks both S and Au.

We have checked the effect that different approximations in DFT may have on μ_S. Results are shown in Table 3, comparing LDA with PBE[51] and optB88.[58,59] The latter accounts for dispersion forces. It can be seen that the order of μ_S for the two complexes is the same for all functionals. For the two higher level theories (PBE and optB88), μ_S values for complexes are lower than those for the p(2 × 2), while for LDA, the reverse is true. Since it is generally believed that generalized gradient approximation (GGA) functionals such as PBE are more accurate than LDA, one should draw the conclusion that the complexes have lower μ_S than the chemisorbed phase according to DFT.

Finally, we note that in our experiments, the sample was prepared at 300 K, and then cooled to 5 K for imaging. After this initial preparation, we regularly re-heated the sample to 300 K and repeated measurements at 5 K, to determine whether observations depended on length of time at 300 K or number

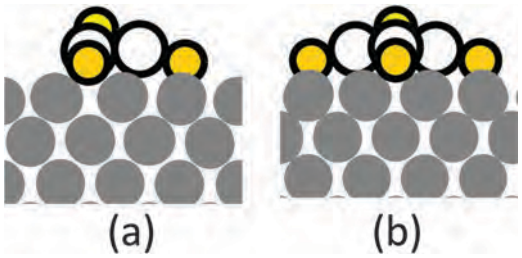

Fig. 12 Cross-sectional views of DFT-optimized configurations for (a) Au_3S_4 and (b) Au_4S_5. The color scheme of Fig. 9 is used.

Table 3 Values of μ_S for different configurations and different approximations in DFT

Configuration	LDA	PBE	optB88
$p(2 \times 2) - S$	−1.998(2) eV	−1.273(2) eV	−1.444(2) eV
$(2\sqrt{2} \times 2\sqrt{2})R45^\circ - AuS_2$	−1.886(15)	−1.327(2)	−1.487(1)
$(2\sqrt{5} \times 2\sqrt{5})R26.6^\circ - Au_4S_5$	−1.942(2)	−1.401(1)	−1.538(1)

of heating–cooling cycles. In all cases, there was no difference in the observations before and after the second cycle. In particular, complexes existed under both conditions, in comparable abundance.

3.4 Mass balance on terraces

Ejected Au atoms can be consumed by Au–S complexes, Au rafts, and (presumably) step edges. From the STM data, we can gain insight into the balance between these pathways. We focus first on large terraces, more than *ca.* 5 nm wide. Fig. 13(a) shows the number density of Au atoms released (calculated from the area of the unreconstructed surface phase), and the density of Au atoms consumed by complexes and Au rafts. Fig. 13(b) shows the fraction of Au atoms that are ejected, but are not accounted for by complexes and rafts. Details of this calculation are given in the ESI.† At the lowest coverage, 80% of the ejected Au is unaccounted for, meaning that it must diffuse to, and be captured at, step edges. For coverages of 0.024 ML or higher, the opposite is true: most of the ejected Au is contained in complexes and Au islands. We interpret this to mean that excess Au cannot diffuse efficiently to nascent step edges at 0.024 ML and above, at 300 K. As the surface becomes more crowded, it becomes more likely that the ejected Au is captured on a terrace before it can reach a step.

Fig. 13(a) also shows that the amount of Au in the complexes is roughly constant as a function of coverage, while the amount of Au in rafts increases significantly, consistent with qualitative observations (*e.g.* Fig. 3).

Terraces narrower than *ca.* 5 nm exhibit very few complexes or rafts. Fig. 14 shows an STM image with several terraces. One, labeled t1, is wide in the lower part of the image, and narrow in the upper part. As it changes from wide to narrow, the complexes/rafts disappear. The other terrace, t2, is narrow throughout and barren. There is also a narrow denuded zone along the upper terrace, next to the step. Such observations mean that the released Au atoms are captured efficiently by step edges at all

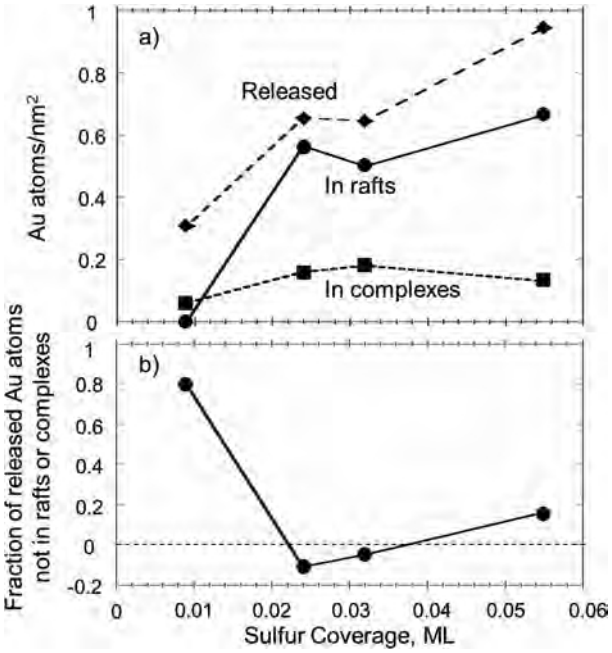

Fig. 13 Mass balance for ejected Au atoms on large terraces. Lines are simply drawn to connect data points. Panel (a) shows the number of Au atoms released and subsequently consumed in S–Au structures, per unit area. Panel (b) shows the fraction of Au atoms not accounted for in observed S–Au structures.

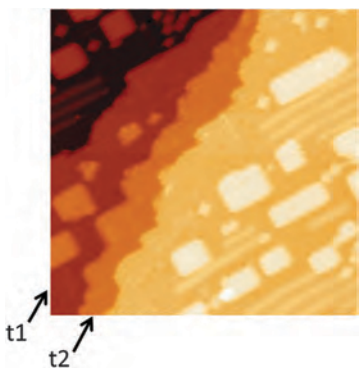

Fig. 14 Topographic STM image including narrow terraces (t1 and t2). 30 × 30 nm^2; 0.12 ML.

S coverages, if the distance to a step is sufficiently small. In turn, this suggests that both complexes and rafts are metastable with respect to steps.

4. Discussion

Nature of the complexes

The main result of this paper is the identification of complexes, primarily Au_4S_5 diamonds, that exist on the unreconstructed Au(100) surface. This is the first observation of metal–sulfur complexes on an fcc(100) surface, to our knowledge. We have isolated these species in experiment by making observations at very low sulfur coverages, in the range 0.009 to 0.12 ML.

A prior study of this system by Jiang *et al.*, using STM and XPS, focused mainly on higher coverages, particularly ordered structures that emerged above 0.25 ML.[31] However, Jiang *et al.* published one STM image where the (unspecified) coverage was considerably below 0.25 ML, since most of the surface was still reconstructed, and another image at a coverage close to 0.25 ML, since the surface was essentially covered by p(2 × 2) islands and rafts. There are many small features in these two images whose shapes are not resolved, but which may be complexes. In fact, in one of the images—the inset to their Fig. 5(b)—a diamond-like shape exists atop a raft.[31] It has an orientation and size consistent with the diamonds reported herein, gauging by the surrounding p(2 × 2) structure.

Formation of four-fold hollow sites for adsorbed S has been proposed to drive reconstructions of the (111) surfaces of Cu[19,20] and Ag,[18] and of the (110) surface of Au.[40] In the present system, however, formation of such sites cannot drive complexation, since the unreconstructed surface already offers four-fold hollow sites. Instead, the stability of the two smaller Au–S complexes, AuS_2 and Au_2S_3, can be attributed to linear S–Au–S (sub)units, *i.e.* staples, as shown in Fig. 9. As noted in Section 1, this motif has been observed previously in Cu–S and Ag–S complexes that form on Cu(111) and Ag(111), respectively.[18,19] In fact, the shape of Au_2S_3 is very analogous to the heart-shaped Cu_2S_3 complex found on Cu(111), where the linear S–Cu–S geometry was shown to maximize overlap between the d_{z^2} orbital of the central metal atom and the p_z orbital of each S atom.[19] As pointed out in Section 3.3 and Fig. 12, the two larger complexes consist of slightly bent S–Au–S subunits. Hence, all the complexes may be regarded as combinations of (near-) linear S–Au–S motifs.

Stabilities of coexisting structures

We have identified the complexes by comparing their size, orientation, and appearance in STM experiments with DFT calculations. We have also identified them on the basis of their favorable μ_S. However, two features of the experimental data are at variance with the DFT. First, the predominance of p(2 × 2) islands and rafts, in experiment, contradicts the fact that μ_S calculated for complexes is lower than that for the p(2 × 2) structure (Section 3.3 and Fig. 8). Second, the fact that μ_S is more negative for the complexes than for the p(2 × 2) phase means that complexes should consume Au atoms from step edges (along with chemisorbed S from terraces), but the data suggest otherwise. In experiment, neither rafts nor complexes are observed on narrow terraces (Section 3.4 and Fig. 14), indicating that both are metastable with respect to step edges. Consistent with the latter premise, Jiang *et al.* reported that annealing at 630 K (starting from a coverage higher than 0.25 ML) produces large domains of p(2 × 2) with no trace of rafts or complexes.[31]

The inconsistency between experiment and DFT could be due to any of several factors. First, DFT may not accurately represent the real system. In particular, our DFT calculations involve an ideal unreconstructed Au(100) substrate. The calculations do not take into account the effects (*e.g.* elastic interactions) of the surrounding reconstruction, nor of the step edges, and such interactions could shift μ_S significantly.

Second, values of μ_S are calculated here for T = 0 K, hence excluding any entropic contribution, whereas the real surface forms at 300 K and quenches at some intermediate temperature as it cools to 5 K. Third, populations of surface species can be predicted from μ_S only if Au atoms on terraces are equilibrated with step edges. This last factor is the only one that can be addressed concretely, since the data show that Au atoms primarily diffuse to step edges if S coverage is very low, or if the terrace is very narrow, but become trapped on terraces under other conditions. Thus, kinetics are considered next.

Kinetics

The kinetics of this system must be very complex, involving diffusion of two different species (Au and S) on different types of Au surfaces (reconstructed and unreconstructed), plus nucleation and growth of complexes and rafts, all combined with the local dynamics of Au atom rearrangement and ejection. In the following, we present some aspects of the kinetics that are known or can be deduced, and then develop a qualitative model that is consistent with key experimental observations.

S can undergo long-range diffusion on the hex phase of Au, at least at 300 K. This is evident from the ability of S atoms to cluster and lift the reconstruction locally, even when the total S coverage is very low, as in Fig. 2. To a first approximation, the diffusion barrier on the hex phase should be comparable to that on Au(111), where its calculated value is 0.39 to 0.47 eV.[37] This is compatible with significant diffusion at room temperature.

At the same time, it is known that Au atom diffusion on the hex phase is anisotropic,[26,60] occurring preferentially in the direction parallel to hex stripes, with a low barrier of 0.32 eV.[26] Its diffusion barrier within a p(2 × 2) matrix of sulfur is presumably much higher. According to DFT, in fact, a single Au atom would form a complex with surrounding sulfur, rather than diffuse.

From our data, and from that of Jiang *et al.*,[31] the initial growth of unreconstructed regions is also highly anisotropic: elongated p(2 × 2) islands form with their long axis parallel to hex stripes. Similar anisotropic growth of unreconstructed regions has been observed for NO, CO, and oxygen on Pt(100),[55,61,62] where it is attributed to the anisotropic degree of commensuration at the interfaces between unreconstructed and hex phases[62] or to anisotropic internal stress in the hex layer.[61] In our observations the hex stripes behave like one-dimensional rods whose ends erode individually as the reconstruction is lifted. This is evident in Fig. 3(a–c), which contains many terminated hex stripes, some marked by arrows.

Close inspection shows that the hex stripes terminate in four ways. The terminus can have no distinctive structure, as in Fig. 3(b) (arrow), or it can be a single dot, as in Fig. 3(c) (arrow). The dot is probably a S adatom. Third, the terminus can be a diamond or partial diamond, as in Fig. 3(a) or Fig. 3(d) (arrows). Good examples are also shown in Fig. 7(d) (lower arrow) and Fig. 7(f) (arrow). In this situation, the complex is actually embedded in the end of the stripe. Fourth, the stripes can end in Au rafts; examples are shown in Fig. 7(d) (upper arrow) and Fig. 7(e) (lower arrow). The fact that complexes and rafts

are found connected to the ends of hex stripes indicates that they may form as a direct result of the local Au structure transformation.

The above features can be combined in the following model—although we do not propose that this model is unique. Excess Au atoms are generated at the ends of stripes. Disposition of these atoms is stochastic. Each atom may diffuse away from the point of generation, or be captured immediately. If a Au atom diffuses away on the hex phase, it moves preferentially parallel to the hex stripes until it is captured. The point of capture can be another unreconstructed island if the terrace is wide or a step edge if the terrace is narrow. When the density of excess Au at a stripe terminus happens to be high while the reconstruction is lifted, a raft forms; when it is moderate, a complex forms; when it is low, p(2 × 2) forms. Once nucleated, rafts can grow indefinitely whereas complexes cannot, which explains why rafts dominate as coverage increases (*cf.* Fig. 13(a)). However at very low coverage, *i.e.* 0.009 ML, only complexes and p(2 × 2) islands can form, because the overall density of excess Au is simply too low to initiate rafts. The Au rafts are metastable; they form only because of the supersaturation of Au adatoms on the (wider) terraces. It is not clear whether the complexes are metastable as well; DFT and experiment are in seeming contradiction on this point. Systematic experiments at higher temperatures could clarify this issue.

5. Conclusions

We have identified a family of related Au–S complexes which form on the Au(100) surface, the most common one being diamond-shaped Au_4S_5. The identification rests on comparisons of their size, shape, and orientation in STM and DFT, together with values of μ_S from DFT. DFT shows that the family of diamond complexes is more stable than other candidate complexes. The formation of complexes, Au rafts, and p(2 × 2) islands is probably competitive and influenced by kinetics under the conditions of these experiments.

Acknowledgements

The experimental component of this work was conducted or supervised by HW, JO, HJY, YK, and PAT. It was supported by three sources. From the U.S., it was NSF Grant CHE-1507223. From Japan, support was provided by a Grant-in-Aid for Scientific Research on Priority Areas ''Electron Transport Through a Linked Molecule in Nano-scale''; and a Grant-in-Aid for Scientific Research(S) ''Single Molecule Spectroscopy using Probe Microscope'' from the Ministry of Education, Culture, Sports, Science, and Technology (MEXT). The theoretical component of this work was carried out by DJL. It was supported by the Division of Chemical Sciences, Basic Energy Sciences, US Department of Energy (DOE). This part of the research was performed at Ames Laboratory, which is operated for the U.S. DOE by Iowa State University under contract No. DE-AC02-07CH11358. This part also utilized resources of the National Energy Research Scientific Computing Center, which is supported by the Office of Science of the U.S. DOE under Contract No. DE-AC02-05CH11231.

References

1 P. J. Feibelman, *Phys. Rev. Lett.*, 2000, **85**, 606–609.
2 P. A. Thiel, M. Shen, D.-J. Liu and J. W. Evans, *J. Vac. Sci. Technol., A*, 2010, **28**, 1285–1298.
3 Z. Shi and N. Lin, *J. Am. Chem. Soc.*, 2009, **131**, 5376–5377.
4 Q. Sun, L. L. Cai, H. H. Ma, C. X. Yuan and W. Xu, *Chem. Commun.*, 2015, **51**, 14164–14166.
5 Q. Fan, T. Wang, L. Liu, J. Zhao, J. Zhu and J. M. Gottfried, *J. Chem. Phys.*, 2015, **142**, 101906.
6 M. Pivetta, G. E. Pacchioni, E. Fernandes and H. Brune, *J. Chem. Phys.*, 2015, **142**, 101928.
7 A. Ulman, *Chem. Rev.*, 1996, **96**, 1533–1554.
8 F. Schreiber, *Prog. Surf. Sci.*, 2000, **65**, 151–257.
9 C. Vericat, M. E. Vela, G. A. Benitez, J. A. Martin Gago, X. Torrellles and R. C. Salvarezza, *J. Phys.: Condens. Matter*, 2006, **18**, R867–R900.
10 C. Vericat, M. E. Vela, G. A. Benitez, P. Carro and R. C. Salvarezza, *Chem. Soc. Rev.*, 2010, **39**, 1805–1834.
11 C. Vericat, M. E. Vela, G. Corthey, E. Pensa, E. Cortes, M. H. Fonticelli, F. Ibanez, G. E. Benitez, P. Carro and R. C. Salvarezza, *RSC Adv.*, 2014, **4**, 27730–27754.
12 J. W. Ndieyira, M. Watari, A. D. Barrera, D. Zhou, M. Vogtli, M. Batchelor, M. A. Cooper, T. Strunz, M. A. Horton, C. Abell, T. Rayment, G. Aeppli and R. A. McKendry, *Nat. Nanotechnol.*, 2008, **3**, 691–696.
13 S. A. DiBenedetto, A. Facchetti, M. A. Ratner and T. J. Marks, *Adv. Mater.*, 2009, **21**, 1407–1433.
14 S. J. Stranick, A. N. Parikh, D. L. Allara and P. S. Weiss, *J. Phys. Chem.*, 1994, **98**, 11136–11142.
15 P. Maksymovych, O. Voznyy, D. B. Dougherty, D. C. Sorescu and J. T. Yates Jr., *Prog. Surf. Sci.*, 2010, **85**, 206–240.
16 H. Häkkinen, *Nat. Chem.*, 2012, **4**, 443–455.
17 R. Ouyang, J. Yan, P. S. Jensen, E. Ascic, S. Gan, D. Tanner, B. Mao, L. Niu, J. Zhang, C. Tang, N. S. Hush, J. R. Reimers and J. Ulstrup, *ChemPhysChem*, 2015, **16**, 928–932.
18 S. M. Russell, Y. Kim, D.-J. Liu, J. W. Evans and P. A. Thiel, *J. Chem. Phys.*, 2013, **138**, 071101.
19 H. Walen, D.-J. Liu, J. Oh, H. Lim, J. W. Evans, C. Aikens, Y. Kim and P. A. Thiel, *Phys. Rev. B: Condens. Matter Mater. Phys.*, 2015, **91**, 045426.
20 H. Walen, D.-J. Liu, J. Oh, H. Lim, J. W. Evans, Y. Kim and P. A. Thiel, *J. Chem. Phys.*, 2015, **142**, 194711.
21 S. Kurokawa, Y. Miyawaki and A. Sakai, *Jpn. J. Appl. Phys.*, 2009, **48**, 08JB12.
22 K. Yamazaki, K. Takayanagi, Y. Tanishiro and K. Yagi, *Surf. Sci.*, 1988, **199**, 595–608.
23 X. Gao, A. Hamelin and M. J. Weaver, *Phys. Rev. B: Condens. Matter Mater. Phys.*, 1992, **46**, 7096–7102.
24 P. Havu, V. Blum, V. Havu, P. Rinke and M. Scheffler, *Phys. Rev. B: Condens. Matter Mater. Phys.*, 2010, **82**, 161418(R).

25 Y. Samson, S. Rousset, S. Gauthier, J. C. Girard and J. Klein, *Surf. Sci.*, 1994, **315**, L969–L972.
26 A. Trembulowicz, G. Ehrlich and G. Antczak, *Phys. Rev. B: Condens. Matter Mater. Phys.*, 2011, **84**, 245445.
27 G. K. Binnig, H. Rohrer, C. Gerber and E. Stoll, *Surf. Sci.*, 1984, **144**, 321–335.
28 D. G. Fedak and N. A. Gjostein, *Surf. Sci.*, 1967, **8**, 77–97.
29 M. A. Van Hove, R. J. Koestner, P. C. Stair, J. P. Bibérian, L. L. Kesmodel, I. BartoŠ and G. A. Somorjai, *Surf. Sci.*, 1981, **103**, 189–217.
30 J. de la Figuera, M. A. González, R. García-Martínez, J. M. Rojo, O. S. Hernán, A. L. V. de Parga and R. Miranda, *Phys. Rev. B: Condens. Matter Mater. Phys.*, 1998, **58**, 1169–1172.
31 Y. Jiang, X. Liang, S. Ren, C.-L. Chen, L.-J. Fan, Y.-W. Yang, J.-M. Tang and D.-A. Luh, *J. Chem. Phys.*, 2015, **142**, 064708.
32 M. Kostelitz, J. L. Domange and J. Oudar, *Surf. Sci.*, 1973, **34**, 431–449.
33 C. Schlaup and K. Wandelt, *Surf. Sci.*, 2015, **631**, 165–172.
34 J. A. Martinez, J. Valenzuela, R. Cao Milan, J. Herrera, M. H. Farias and M. P. Hernandez, *Appl. Surf. Sci.*, 2014, **320**, 287–293.
35 T. Ślusarski and T. Kostyrko, *Surf. Sci.*, 2009, **603**, 1150–1155.
36 A. D. Daigle and J. J. BelBruno, *J. Phys. Chem. C*, 2011, **115**, 22987–22997.
37 H. Walen, D.-J. Liu, J. Oh, H. Lim, J. W. Evans, Y. Kim and P. A. Thiel, *J. Chem. Phys.*, 2015, **143**, 014704.
38 S. M. Russell, M. Shen, D.-J. Liu and P. A. Thiel, *Surf. Sci.*, 2011, **605**, 520–527.
39 D.-J. Liu, H. Walen, J. Oh, H. Lim, J. W. Evans, Y. Kim and P. A. Thiel, *J. Phys. Chem. C*, 2014, **118**, 29218–29223.
40 H. Walen, D.-J. Liu, J. Oh, H. J. Yang, Y. Kim and P. A. Thiel, *J. Phys. Chem. C*, 2015, **119**, 21000–21010.
41 C. Wagner, *J. Chem. Phys.*, 1953, **21**, 1819–1827.
42 D. Detry, J. Drowart, P. Goldfinger, H. Keller and H. Rickert, *Z. Phys. Chem.*, 1967, **55**, 314–319.
43 W. Heegemann, K. H. Meister, E. Bechtold and K. Hayek, *Surf. Sci.*, 1975, **49**, 161–180.
44 A. Maeland and T. B. Flanagan, *Can. J. Phys.*, 1964, **42**, 2364–2366.
45 D. Gibbs, B. M. Ocko, D. M. Zehner and S. G. J. Mochrie, *Phys. Rev. B: Condens. Matter Mater. Phys.*, 1990, **42**, 7330–7344.
46 S. G. J. Mochrie, D. M. Zehner, B. M. Ocko and D. Gibbs, *Phys. Rev. Lett.*, 1990, **64**, 2925–2928.
47 G. Kresse and J. Furthmüller, *Phys. Rev. B: Condens. Matter Mater. Phys.*, 1996, **54**, 11169–11186.
48 G. Kresse and J. Hafner, *Phys. Rev. B: Condens. Matter Mater. Phys.*, 1994, **49**, 14251–14269.
49 G. Kresse and J. Hafner, *Phys. Rev. B: Condens. Matter Mater. Phys.*, 1993, **47**, 558–561.
50 G. Kresse and D. Joubert, *Phys. Rev. B: Condens. Matter Mater. Phys.*, 1999, **59**, 1758–1775.
51 J. P. Perdew, K. Burke and M. Ernzerhof, *Phys. Rev. Lett.*, 1996, **77**, 3865–3868.
52 D.-J. Liu, *Phys. Rev. B: Condens. Matter Mater. Phys.*, 2010, **81**, 035415.
53 J. Tersoff and D. R. Hamann, *Phys. Rev. Lett.*, 1983, **50**, 1998–2001.
54 J. Liu, C.-W. Wu and T. T. Tsong, *Phys. Rev. B: Condens. Matter Mater. Phys.*, 1991, **43**, 11595–11604.
55 A. Borg, A. M. Hilmen and E. Bergene, *Surf. Sci.*, 1994, **306**, 10–20.
56 G. Ritz, M. Schmid, P. Varga, A. Borg and M. Ronning, *Phys. Rev. B: Condens. Matter Mater. Phys.*, 1997, **56**, 10518–10525.
57 P. Bak, P. Kleban, W. Unertl, J. Ochab, G. Akinci, N. C. Bartelt and T. L. Einstein, *Phys. Rev. Lett.*, 1985, **54**, 1539–1542.
58 J. Klimes, D. R. Bowler and A. Michaelides, *J. Phys.: Condens. Matter*, 2010, **22**, 022201.
59 J. Klimes, D. R. Bowler and A. Michaelides, *Phys. Rev. B: Condens. Matter Mater. Phys.*, 2011, **83**, 195131.
60 S. Günther, E. Kopatzki, M. C. Bartelt, J. W. Evans and R. J. Behm, *Phys. Rev. Lett.*, 1994, **73**, 553–556.
61 E. Ritter, R. J. Behm, G. Potschke and J. Wintterlin, *Surf. Sci.*, 1987, **181**, 403–411.
62 K. Mase and Y. Murata, *Surf. Sci.*, 1992, **277**, 97–108.

Supplemental Information for

Identification of Au-S complexes on Au(100)

Holly Walen, Da-Jiang Liu, Junepyo Oh, Hyun Jin Yang, Yousoo Kim, and P. A. Thiel

1. Tunneling conditions for STM images in the main text.

Figure	Image size (nm^2)	Tunneling current (nA)	Sample Bias (V)	θ_S
1a	30 x 30	0.915	-0.516	
1b	10 x 10	8.72	-0.002	
1c	5 x 5	13.91	-0.002	
2a	8 x 8	2.19	-0.456	0.009
2b	10 x 10	1.83	-0.500	0.009
2c	10 x 10	2.63	-0.002	0.009
2d	10 x 10	2.85	-0.002	0.009
3a	15 x 15	1.72	-0.085	0.024
3b	15 x 15	1.94	-0.052	0.032
3c	15 x 15	2.38	-0.078	0.055
3d	15 x 15	1.01	-0.061	0.115
4a	15 x 15	1.68	-0.135	0.009
4b	15 x 15	2.104	-0.038	0.032
6a	5 x 3.3	3.03	-0.023	0.055
6b	10 x 10	1.91	-0.229	0.009
6c	10 x 10	1.00	-1.000	0.009
6d	10 x 10	3.03	-0.023	0.055
6e	10 x 10	1.68	-0.253	0.055
6f	10 x 10	1.79	-0.168	0.055
6g	10 x 10	2.10	-0.038	0.055
8e	3.6 x 4	0.468	+1.000	0.115
9a	2 x 2	2.91	-0.033	0.055
9b	2 x 2	3.03	-0.023	0.055
9c	2 x 2	2.10	-0.038	0.055
12	30 x 30	1.75	+0.092	0.115

2. Details of determining Au mass balance.

The density of atoms in the hex reconstruction, N_{hex}, is 15 nm^{-2}, while in the unreconstructed layer the density, N_{1x1}, is 12 nm^{-2}. To determine the number of ejected Au atoms, we first determine the area of the unreconstructed regions and multiply this by the density difference, ΔN = 3 nm^{-2}. This gives the density of Au atoms released, N_{rel}. Then, we evaluate the density of Au atoms contained in complexes and rafts, N_{cr}. If there were perfect mass balance on the terrace (and within the scope of the imaged regions), the difference N_{rel} - N_{cr} would be zero.

The fraction of Au atoms released but not accounted for in complexes and rafts, shown in Fig. 13(b), is calculated as $F = (N_{rel} - N_{cr})/ N_{rel}$. A positive value of F indicates that more Au atoms are ejected than consumed, as is true at 0.009 ML. A large negative value of F would indicate the reverse. We estimate that the small deviations of F from zero, at 0.024, 0.032, and 0.055 ML in Fig. 13, are within experimental uncertainty.

3. Details of DFT results for the chemisorbed phases.

Energetics of single S adsorbed on 4fh sites of Au(100) in 9 different supercells from DFT-PBE calculations, averaging from L = 7 to 12. Uncertainties, in parentheses, represent the variation in μ_S between individual slab thickness values. The index j is the separation between nearest-neighbor S atoms in units of a, for each supercell. The three values in boldface define the convex hull shown in Fig. 4 in the text.

j	θ_S	k-points grid	Supercell	μ_S (eV)
1	1	(12 x 12)	(1 x 1)	0.169(4)
2	**1/2**	**(17 x 17)**	**(√2 x √2)R45°**	**-0.834(2)**
3	**1/4**	**(12 x 12)**	**(2 x 2)**	**-1.273(2)**
4	1/5	(11 x 11)	(√5 x √5)R26.6°	-1.219(4)
5	1/8	(8 x 8)	(2√2 x 2√2)R45°	-1.282(5)
6	1/9	(8 x 8)	(3 x 3)	-1.268(2)
7	1/10	(8 x 8)	(√10 x √10)R18.4°	-1.281(2)
8	**1/13**	**(7 x 7)**	**(√13 x √13)R33.7°**	**-1.294(5)**
9	1/16	(6 x 6)	(4 x 4)	-1.285(3)

4. Other configurations evaluated with DFT.

Figures S1-S9 show some of the other S atom arrays tested in DFT. Each panel contains a schematic of the repeating structure within the unit cell, slab thickness (L), and the chemical potential of sulfur, μ_S. Many panels also include a simulated STM image, in shades of orange. The supercell is given in each figure caption.

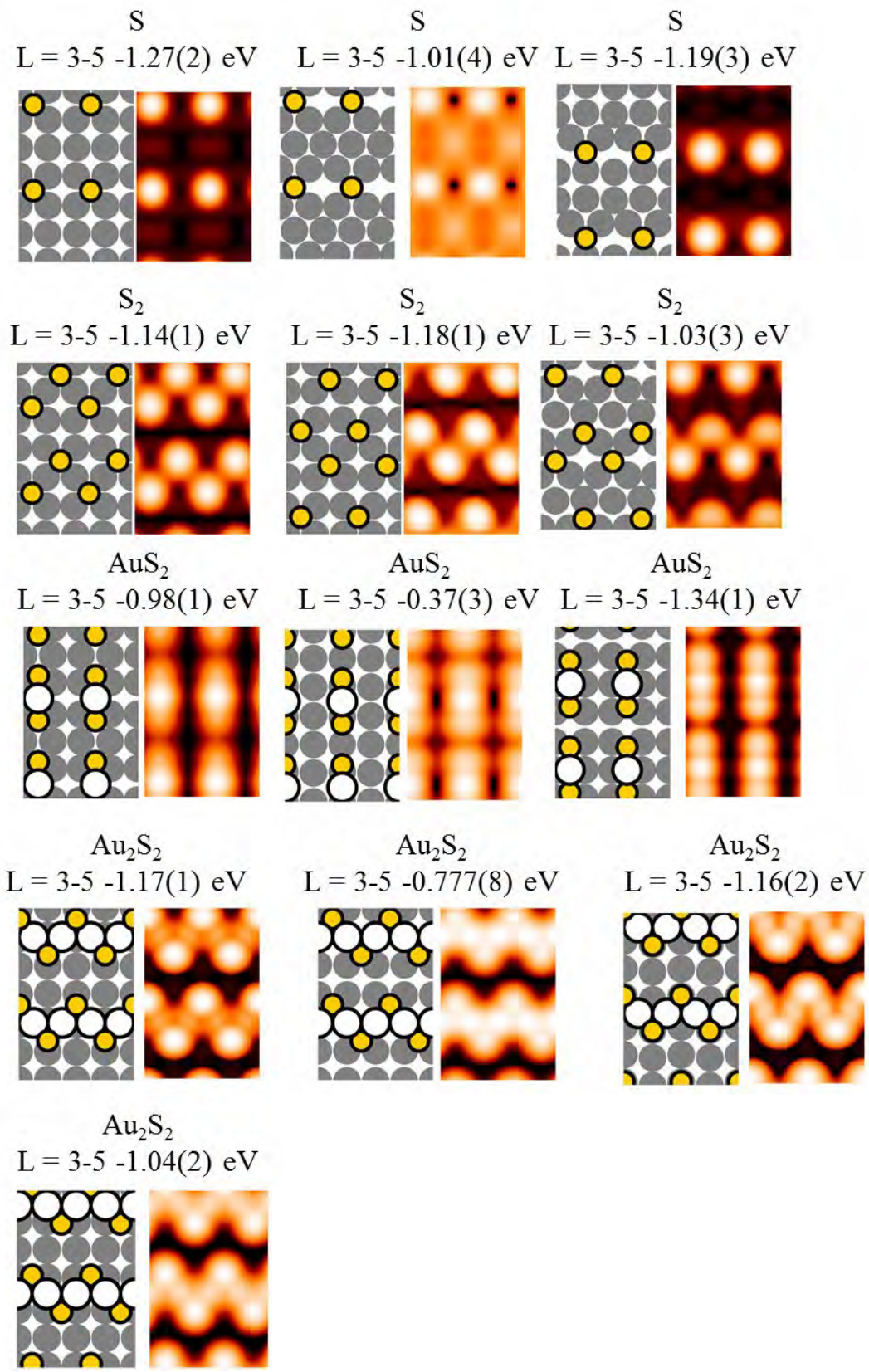

Figure S1. (2 x 3) supercell.

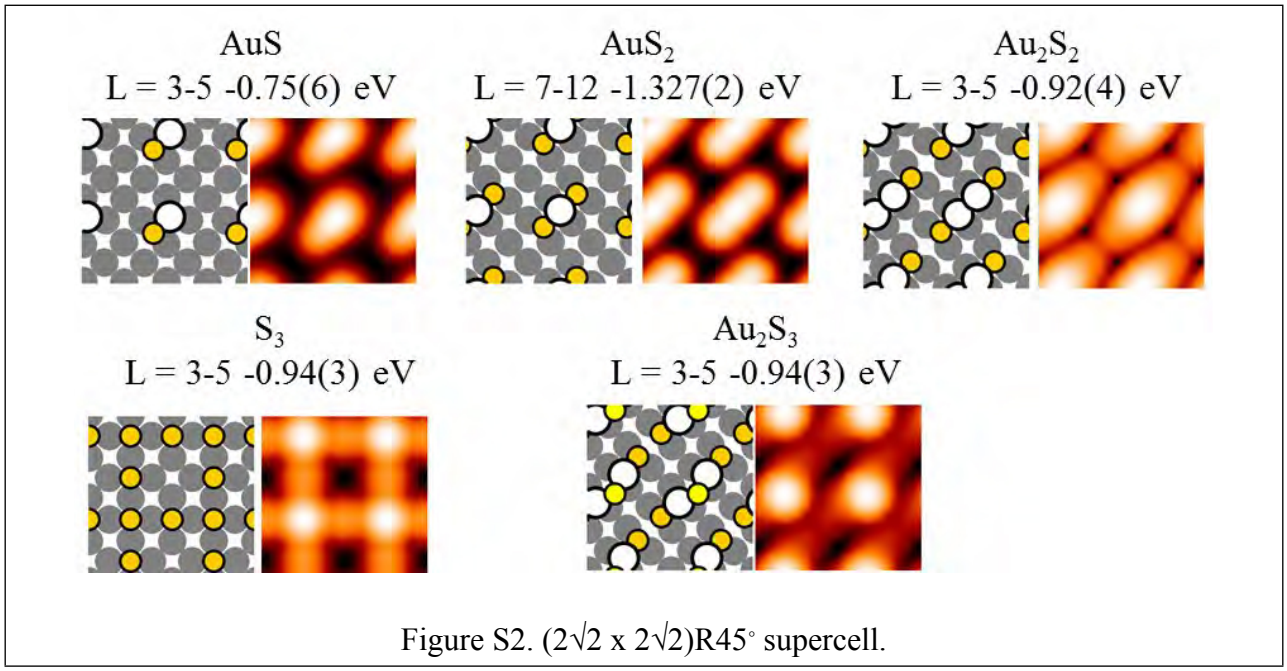

Figure S2. (2√2 x 2√2)R45° supercell.

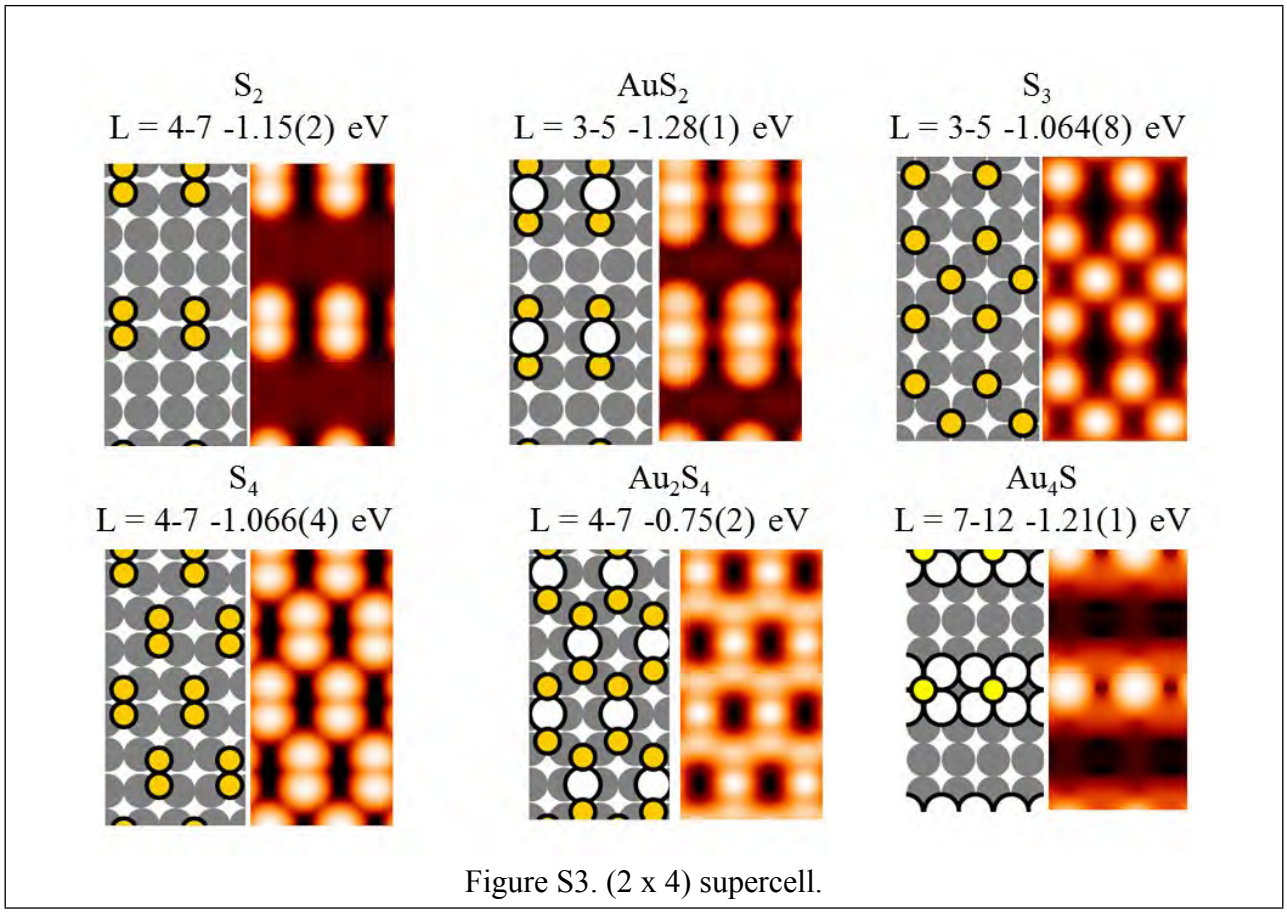

Figure S3. (2 x 4) supercell.

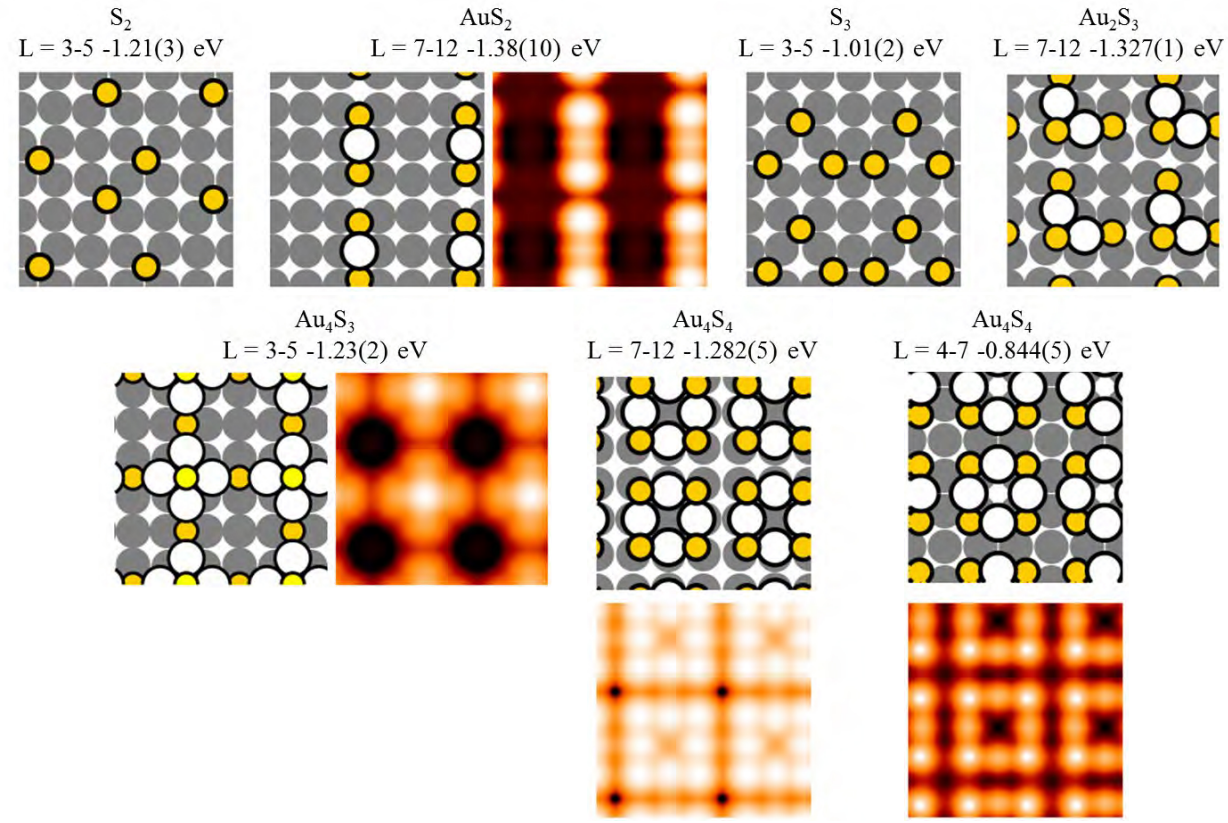

Figure S4. (3 x 3) supercell.

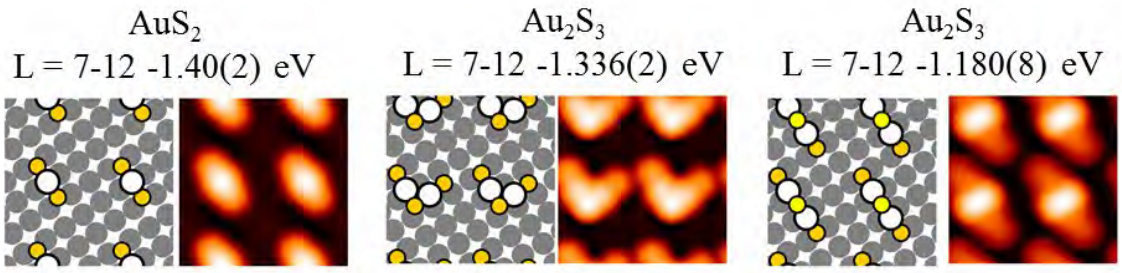

Figure S5. (√13 x √13)R33.7° supercell.

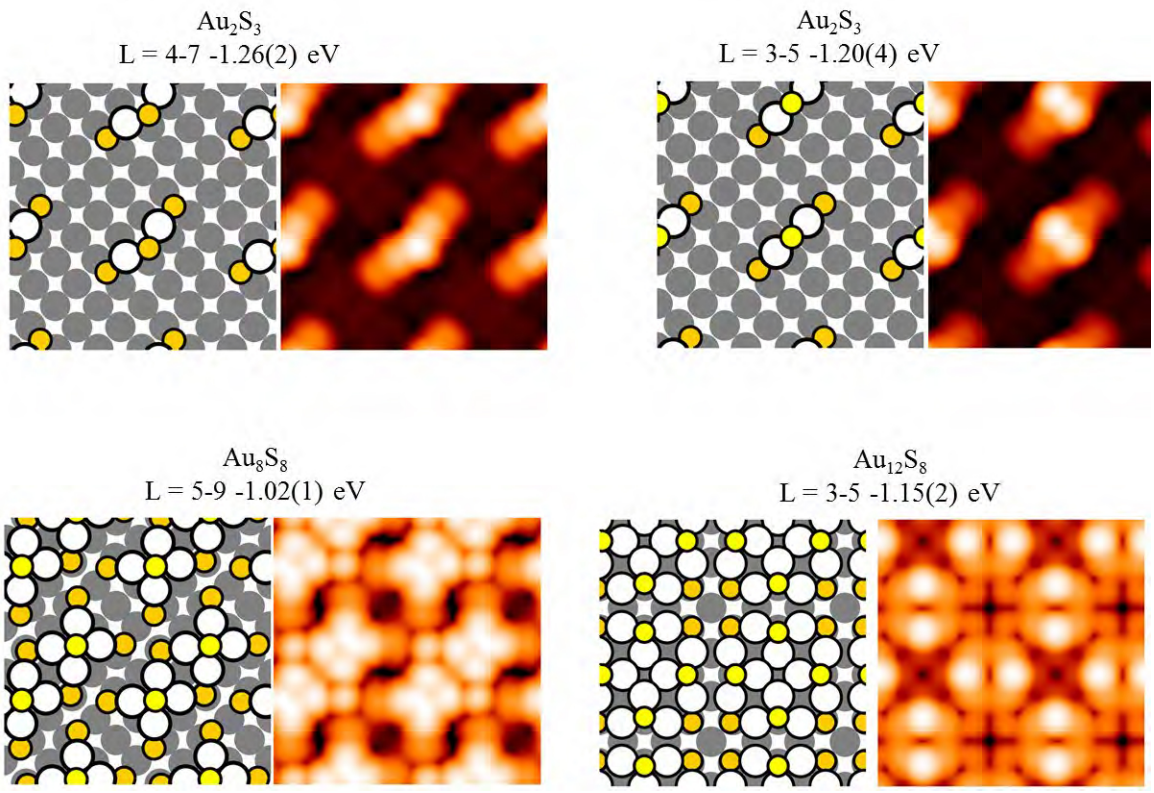

Figure S6. (3√2 x 3√2)R45° supercell.

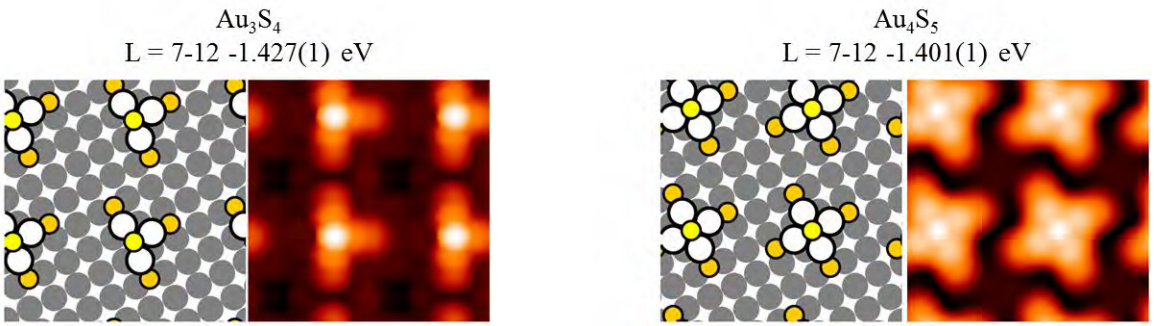

Figure S7. (2√5 x 2√5)R26.6° supercell.

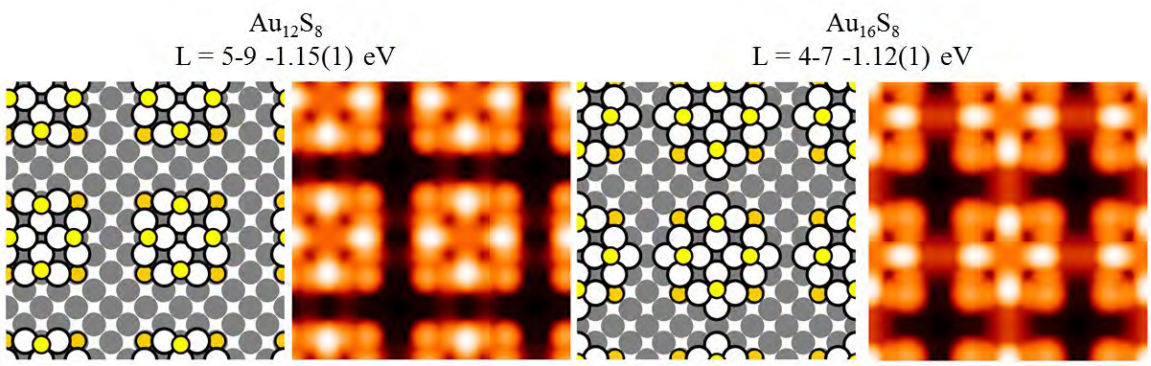

Figure S8. (4√2 x 4√2)R45◦ supercell.

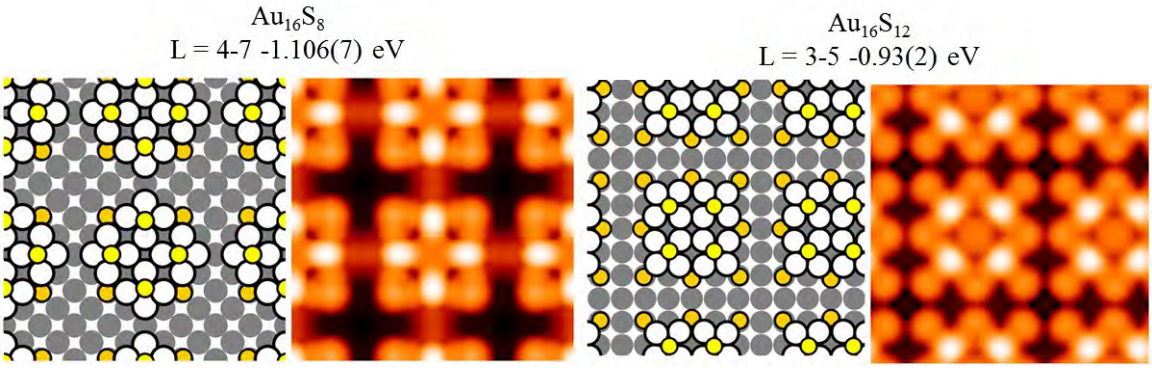

Figure S9. (6 x 6) supercell.